Journal of Power Sources 688 (2026) 240481

Contents lists available at ScienceDirect

Journal of Power Sources

journal homepage: www.elsevier.com/locate/jpowsour

Influence of slurry drying machinery conditions on lithium-ion battery cathode microstructural properties: Multiscale modelling insights

Abhilash Valisammagari [a,b], Francisco Fernandez [a,b], Mohammed Alabdali [a,b], Alejandro A. Franco [a,b,c,d,*]

[a] Laboratoire de Réactivité et de Chimie des Solides, UMR CNRS 7314, Université de Picardie Jules Verne, Amiens Cedex, 80039, France
[b] Réseau sur le Stockage Electrochimique de l'Energie (RS2E), Hub de l'Energie, FR CNRS, 15 rue Baudelocque, Amiens Cedex, 80039, France
[c] ALISTORE-European Research Institute, Hub de l'Energie, FR CNRS 3104, 15 Rue Baudelocque, Amiens Cedex, 80039, France
[d] Institut Universitaire de France, 103 Boulevard Saint Michel, Paris, 75005, France

HIGHLIGHTS

- A multiscale model linking drying machine settings to electrode microstructures.
- Local variations of airflow in the dryer can lead to non-uniform drying.
- High drying rates induce binder migration towards the surface.
- The internal pore structure naturally limits the free movement of binder.
- Balanced drying conditions optimise electrode microstructure and performance.

ARTICLE INFO

Keywords:
Li-ion batteries
Manufacturing process
Slurry drying
Coating heterogeneities
Multiscale modelling

ABSTRACT

The performance of lithium-ion battery (LIB) electrodes is significantly influenced by the manufacturing parameters selected during their production. A key step involving high energy consumption and cost is the slurry drying. This stage can cause the carbon additive and binder to undesirably migrate across the electrode thickness, reducing electrochemical performance and durability during LIB cell operation. This study introduces a novel modelling approach that couples multiple scales in order to address the impact of heterogeneous drying conditions on the microstructure of dried electrodes. The framework integrates a macroscale model of the drying machine with a 3D mesoscale model to predict the final microstructural properties across the electrode film. These models are interconnected by a 1D model that monitors local solvent evaporation and drying time. This novel methodology allows for a detailed investigation into how variations in chamber temperature influence binder migration. As a proof-of-concept, this framework demonstrates that the drying stage in pilot lines involves heterogeneities that result in variable drying rates across the slurry film. The reported methodology also quantifies the extent of in-plane variability in electrode properties resulting from drying heterogeneities, providing key insights for process optimisation.

1. Introduction

Lithium-ion batteries (LIBs) are widely recognised as the leading secondary energy storage technology due to their extensive application in portable electronic devices and electric vehicles. The rapidly growing global demand for LIBs has intensified the requirements for higher energy and power densities, a longer cycle life, and enhanced efficiency, all while simultaneously lowering production costs. A critical pathway towards achieving these objectives lies in the optimisation of the electrode manufacturing process, which directly influences its performance [1]. Electrode fabrication involves multiple sequential steps: (i.) preparation of the slurry by mixing active material (AM), conductive additives, and binder in a solvent, (ii.) coating onto a current collector, (iii.) drying to remove the solvent, and (iv.) calendering to densify the electrode. Each stage of electrode fabrication dictates its microstructure, and consequently, its performance through the parameters chosen in each

* Corresponding author.
E-mail address: alejandro.franco@u-picardie.fr (A.A. Franco).

https://doi.org/10.1016/j.jpowsour.2026.240481
Received 25 February 2026; Received in revised form 27 April 2026; Accepted 20 May 2026
Available online 10 June 2026

one of the steps. Among these, the drying step is the one that consumes the most energy and incurs the highest costs, accounting for approximately 46 % of the total energy consumption and 20-25 % of the capital expenditure in the entire manufacturing process of the electrode [2–5].

Conventionally, the drying of electrode slurries is performed by convective heating, where hot air is passed over the slurry film surface to induce solvent evaporation. In this case, the drying process generally proceeds in two distinct stages [6]. The initial constant-rate period is characterised by stable surface evaporation of the solvent. In this stage, the liquid-air interface recedes steadily into the coating, and the particles rearrange until they reach a locking configuration that forms the particulate skeleton [6,7]. At the end of this stage, the thickness of the film converges, which is referred to as the end of film shrinkage. This is followed by the falling-rate period, where solvent is removed from the porous network via capillary forces and the sequential emptying of pores (starting with the larger ones and following with smaller ones). Because solvent mobility is restricted and heterogeneities in pore structure may generate lateral stresses, the falling-rate stage is often kinetically limiting and governs the overall drying time [8].

The drying kinetics are strongly linked to the degradation of the electrode performance. High drying rates promote the movement of non-volatile components by advection, leading to a phenomenon known as migration or stratification [9–12]. This results in the undesirable accumulation of binder and conductive additives near the electrode surface and their depletion closer to the current collector. This segregation causes several defects that limit the performance of the electrodes, such as, poor adhesion of AM to the current collector, reduced mechanical stability, and pore clogging that impedes ion transport [13,14]. Such heterogeneities increase the electrode resistance due to insufficient ionic and electronic conductive pathways. This ultimately limits the capacity and rate capability of the electrode.

Although the impact of drying rates on the migration of conductive additives, and the subsequent impact on the electrochemical performance, was investigated using several experimental techniques [12–16], studies resolving the electrode microstructural evolution during drying remain scarce and technically challenging [15,17–20]. Methods such as cryogenic broad ion beam scanning electron microscopy (cryo-BIB-SEM) have successfully visualised binder migration, but their technical complexity limits their application for transient, high-throughput analysis [20]. These limitations give rise to some open questions that can be addressed using physics-based modelling techniques.

Existing physics-based modelling efforts have largely focused on mesoscale transport phenomena, which describe the bulk movement of solvent, heat, and dissolved components across the electrode thickness [8,9,19,21–24]. These models have simplified the drying kinetics by using one-dimensional (1D) approximation across the coating thickness. These approaches rely on solving coupled equations, primarily the convection-diffusion equation for solvent transport and a 1D heat transfer equation. For instance, models have characterised binder migration using Peclet numbers to quantify the competition between advective and diffusive effects [25], compared different solvent systems [26], and analysed optimal drying profiles for binder migration [9]. Other implementations in the 1D approximation have incorporated solvent-polymer interaction kinetics to predict the decay of the solvent diffusion coefficient and evaporation rates, known as Flory-Huggins activation coefficients [21]. All the previous works were addressing the constant-rate period of the drying stage. During the falling-rate period, when vapor and liquid transport occurs within the porous network, approaches have included saturation parameters to describe phase distribution [8] or extended linear drying kinetics with a moving drying front model to approximate the internal mass transport resistance of thicker electrodes [22,23]. Nevertheless, none of these approaches have explicitly resolved in 3D the arrangements of the particles, and how they are affected during the different drying stages with varying parameters.

To provide a more detailed description of the microstructure during the drying step, we have developed particle-based models to address the spatial arrangement of its internal components [10,27–29]. These models are based on the Coarse-Grained Molecular Dynamics (CGMD) and discrete element method (DEM), where the AM particles, the carbon additives, the binder, and the solvent are spatially described to obtain the microstructural evolution during different manufacturing steps, including drying. In the early stages of the drying process, the carbon additives, binder, and solvent are represented by a single type of particle referred to as a carbon-binder-solvent aggregate (CBSA). After the solvent evaporates, the carbon additives and binder are represented by a single carbon-binder domain (CBD) particle. These models are essential for understanding how the final electrode microstructure is formed and how segregation manifests at the electrode level, by allowing to link manufacturing steps through the microstructure and the influence of various parameters. These models were developed in the context of our ARTISTIC research initiative [30], which involves designing physics-based models for key manufacturing steps to digitally represent the manufacturing process chain of LIB electrodes. These models have been calibrated and validated using experimental data [31]. Furthermore, they were also used to generate datasets that have proved to be suitable to train artificial intelligence (AI) surrogate models that represent the interdependencies between the manufacturing parameters and the electrode properties [28,32–34].

Particularly for the drying stage, we have previously defined different drying rates based on the initial distribution of CBSA particles. We also studied the impact of drying rate heterogeneities on the migration of CBD and the microstructure formation by considering spherical AM particles [10]. This later assumption was then improved in the work of Xu et al. [27], where realistic-shape AM particles, coming from tomography determinations, were introduced to study homogeneous drying by gradually reducing the slurry thickness. Furthermore, we have coupled this mesoscale model with deep learning predictions in a hybrid approach, referred to as physics-assisted machine learning (ML), which allowed us to determine a compromise between prediction accuracy and computational cost [28,33].

In this work, we present a novel multi-scale, multi-physics modelling approach that enables the analysis and prediction of how macroscopic heterogeneities in dryer machines at the pilot line scale influence the internal microstructure at different locations of the electrode film. Resolving microstructural details throughout the dryer is computationally challenging. Therefore, a multi-scale, one-way coupling strategy is proposed (see the schema presented in Fig. 1). First, we perform macroscale simulations to capture the spatial variations of the drying conditions (in terms of air temperature and velocity) inside a drying machine. The resulting local evolution data is then used to model the kinetics of the drying and to transfer the solvent content and drying time to the electrode mesoscale model. This model is then used to predict the microstructural properties at different regions of the dried electrode. To the best of our knowledge, this is the first time such an approach is proposed for this stage of the electrode manufacturing process and involving these levels of detail. Here, we systematically use it by setting different temperature configuration for inlet air in a dual chamber dryer machine. We set different temperatures in the macroscale model for the first dryer (343 K, 343 K, 373 K), combined with different ones in the second dryer (373 K, 393 K, 393 K), giving the following combinations: 343-373 K, 343-393 K, and 373-393 K. For these three air temperature configurations, the 1D model captures the solvent concentration profile across three regions of the slurry film: the edge region, the intermediate region and the central region. The intermediate region refers to the zone located between the central and the edge regions of the slurry film. These heterogeneities are then used as inputs in our mesoscale model to resolve in 3D and as a function of time the arrangement of the particles (AM and CBD), to analyse how these variations affect the binder migration. Finally, we calculate different electrode properties (such as porosity, tortuosity factor, and conductivity) across the different regions of the slurry film and for the different initial slurry microstructures, and

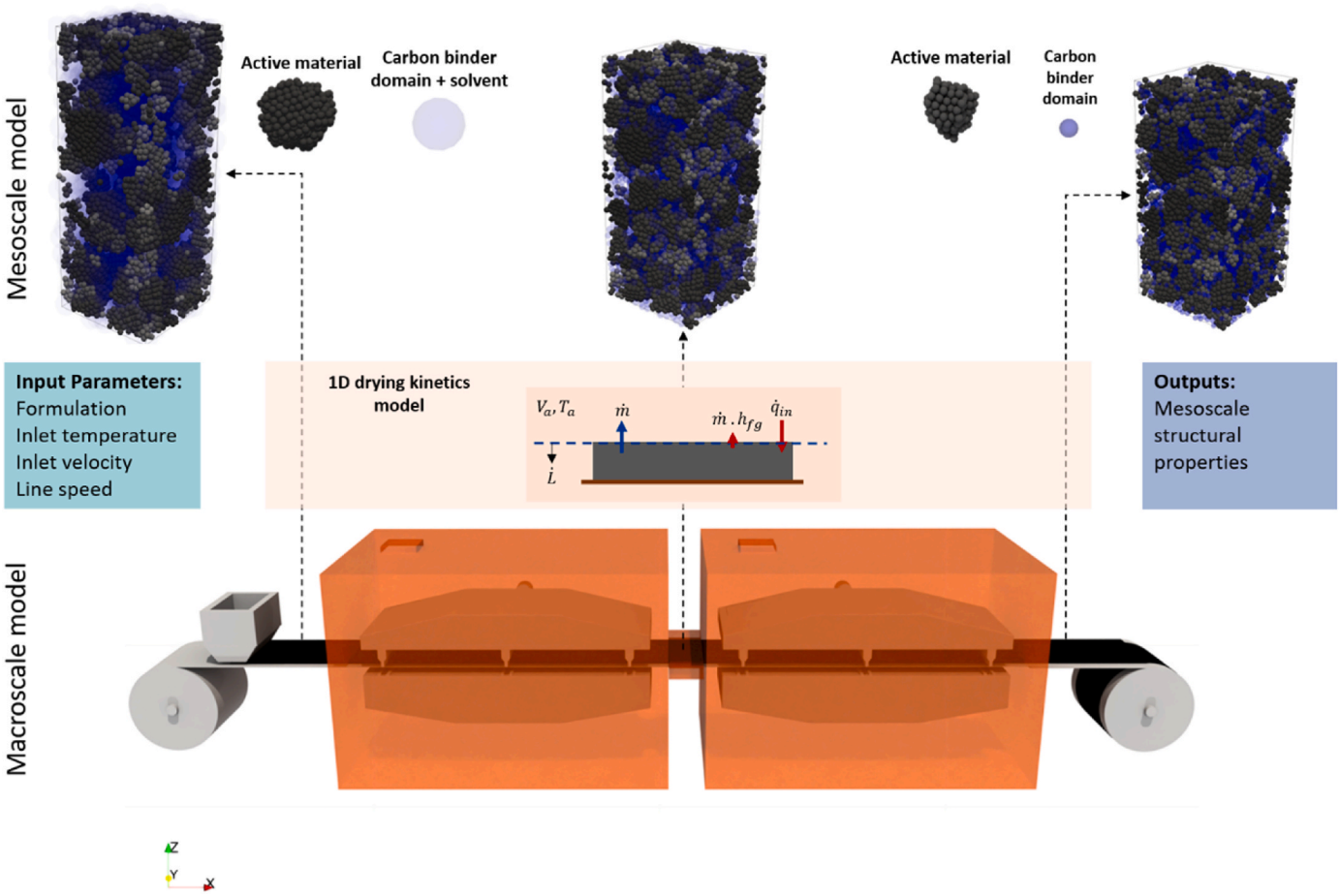

Fig. 1. Schematic of the proposed workflow of the multi-physics modelling framework composed of multiple scales. The hierarchy integrates a macroscale pilot line dryer (bottom) with a 3D mesoscale coarse-grained molecular dynamics (CGMD) model (top three microstructures), which captures the morphological evolution of active material (AM) and carbon-binder domain (CBD) particles during drying. These models on different scales are interconnected through a 1D drying kinetics model (centre) that governs the solvent evaporation rates and drying dynamics.

analyse how the air temperature configurations set in the macroscale model affects their average behaviour. For the demonstration of our approach, we used a slurry formulation composed of LiNiMnCoO (NMC111) cathode AM, carbon black, Polyvinylidene fluoride (PVdF) binder dispersed in the N-methyl-2-pyrrolidone (NMP) solvent. The article is organised as follows: Section 2 presents the computational methodology, detailing the models and numerical approaches employed. Section 3 discusses the simulation results on heterogeneities and their implications. Finally, Section 4 provides a summary of key findings and outlines directions for future research.

2. Methodology

In this section, we present the details of our proposed modelling approach, that links the macroscopic drying conditions within the dual chamber of a pilot line dryer to the resulting microstructure of the slurry at the mesoscale. First, we present the macroscale Computational Fluid Dynamics (CFD) model, followed by the 1D kinetics model, and finally the mesoscale CGMD model.

2.1. Macroscale model for the dryer flow conditions

To study the variations in the hot air flow inside the dryer chamber of the pilot line (Fig. 1), CFD simulations were conducted using OpenFOAM software [35], with the conjugate heat transfer solver. This solver simultaneously resolves the Navier-Stokes equations in the fluid region and the heat conduction equations in the solid region. The governing equations solving for the temperature, velocity, and pressure fields within the fluid region are the continuity equation for the conservation of mass in the fluid flow,

$$\frac{\partial \rho}{\partial t} + \nabla \cdot (\rho u) = 0 \qquad \text{Equation 1}$$

the momentum conservation equation for the fluid,

$$\frac{\partial (\rho u)}{\partial t} + \nabla \cdot (\rho (u \otimes u)) = -\nabla p + \nabla \cdot \tau + \rho g \qquad \text{Equation 2}$$

and the energy conservation equation for the fluid,

$$\frac{\partial (\rho h)}{\partial t} + \nabla \cdot (\rho u h) = \nabla \cdot (\lambda \nabla T) + S \qquad \text{Equation 3}$$

where, ρ [kg·m^{-3}] is the density, u [m·s^{-1}] is the fluid velocity, p [Pa] is the pressure, τ [Pa] represents the viscous and turbulent stresses, g [m·s^{-2}] is the acceleration due to gravity, h [J·kg^{-1}] is the enthalpy, λ [W·m^{-1}·K^{-1}] is the thermal conductivity, T [K] is the temperature, and S is the source term for energy.

Additionally, in the solid domain, the energy conservation equation simplifies to a heat conduction equation to be solved for its temperature:

$$\frac{\partial (\rho c_p T)}{\partial t} = \nabla \cdot (\lambda \nabla T) + S \qquad \text{Equation 4}$$

where, C_p [J·kg^{-1}·K^{-1}] is the specific heat capacity at constant pressure for the solid material.

Temperature and flux continuity are imposed at the interface between the solid and fluid regions.

This macroscale CFD simulation provides spatially and temporally resolved velocities and temperatures of the hot air inside the dryer. The convective heat transfer coefficient, h_t [W·m^{-2}·K^{-1}], corresponding to the velocity and temperature profiles is estimated using correlations for forced convection of hot air over a flat plate [8],

$$h_t = 0.037\, v_a^{0.8} \left(\frac{\mu_a}{\rho_a}\right)^{-0.8} P_r^{(1/3)} \lambda_a L_{ch}^{-0.2} \quad \text{Equation 5}$$

where, v_a [m·s^{-1}] is the air velocity, μ_a [Pa·s] its dynamic viscosity, ρ_a [kg·m^{-3}] its density, λ_a [W·m^{-1}·K^{-1}] its thermal conductivity, L_{ch} [m] its characteristic length, and Pr [−] the Prandtl number, which characterises the relative thickness of velocity and thermal boundary layers and is expressed as

$$Pr = \frac{C_{p_a} \cdot \mu_a}{\lambda_a} \quad \text{Equation 6}$$

where C_{p_a} [J·kg^{-1}·K^{-1}] is the heat capacity. The corresponding mass transfer coefficient, k_c [m·s^{-1}], is computed using the Chilton-Colburn analogy that links the heat and mass transfer coefficients [8],

$$\boldsymbol{k_c} = \frac{\boldsymbol{h_t}}{\left(\boldsymbol{\rho_a c_{P_a}} \mathrm{Le}^{2/3}\right)} \quad \text{Equation 7}$$

where, Le [−] is the Lewis number that describes the relative rates of thermal and mass diffusion, and is expressed as,

$$\boldsymbol{Le} = \frac{\boldsymbol{Sc}}{\boldsymbol{Pr}} = \frac{\boldsymbol{\mu_a}}{\boldsymbol{\rho_a D_a}} \frac{\boldsymbol{1}}{\boldsymbol{Pr}} \quad \text{Equation 8}$$

with Sc [−] the Schmidt number and D_a [m^2·s^{-1}] the mass diffusivity of solvent vapor in air. The convective heat and mass transfer coefficients estimated from Equation (5) and Equation (7) correspond to flat-plate correlations. The validity and impact of this assumption are further discussed in Section 3.

2.2. 1D drying kinetics model

The drying kinetics model is computed at discrete locations along the film path and takes the time-evolving transfer coefficients from the macroscale model as inputs. Then, as an output, it gives the local, time-dependent profile of solvent removal. The drying of the film at this level of description is modelled following the framework presented by Oppegård et al. [21]. This model is suitable during the constant-rate drying, since the two-phase transport (of vapor and liquid phases of the solvent in pores), occurring in the falling-rate period, is not explicitly accounted for. However, in this model, the limitations of the solvent transport in the falling-rate period are approximated using the solvent fraction-dependent transport properties. As a result of this approximation, this model is suitable only for thin coatings, where the tortuous network for two-phase flow is relatively short. Conversely, for thicker films, two-phase transport and migration due to capillary forces cannot be neglected. In the centre of Fig. 1, we illustrate the coupled heat and mass transfer phenomena between the slurry film and the drying environment. The following drying kinetics model is implemented in COMSOL® software.

2.2.1. Solvent transport

The solvent transport within the film is assumed to occur solely by diffusion. The concentration profile is therefore described by the 1D diffusion equation, given by the Fick's second law, which assumes that no reactions are occurring as presented in Equation (9):

$$\frac{\partial \boldsymbol{C}}{\partial \boldsymbol{t}} = \frac{\partial}{\partial \boldsymbol{z}} \left(\boldsymbol{D_{eff}} \frac{\partial \boldsymbol{C}}{\partial \boldsymbol{z}}\right) \quad \text{Equation 9}$$

where, C [mol·m^{-3}] is the concentration of the solvent in the slurry and D_{eff} [m^2·s^{-1}] is the effective diffusion coefficient of the solvent in the solvent polymer mixture and varies with the slurry temperature as [21, 24]

$$\boldsymbol{D_{eff}} = \boldsymbol{D_0} \left(\frac{\boldsymbol{1 - \Phi_p}}{\boldsymbol{1 + \Phi_p}}\right)^{\gamma} \boldsymbol{exp}\left(\frac{\boldsymbol{-E_a}}{\boldsymbol{RT}}\right) \quad \text{Equation 10}$$

where, D_0 [m^2·s^{-1}] is the polymer solvent mutual diffusion coefficient, Φ_p [−] is the polymer volume fraction, γ [−] is the empirical constant describing the nonlinearity in evolution of diffusion coefficient, E_a [J·mol^{-1}] is the activation energy, R [J·mol^{-1}·K^{-1}] is the universal gas constant, and T [K] is the film temperature. Qualitatively speaking, Equation (10) for D_{eff} tends to zero as the solvent is completely removed, which represents the expected behaviour of the components.

The bottom boundary of the slurry coating (at $z = 0$) is impermeable, leading to a zero-flux condition,

$$\boldsymbol{D_{eff}} \frac{\partial \boldsymbol{C}}{\partial \boldsymbol{z}} = \boldsymbol{0} \quad \text{Equation 11}$$

and for the slurry film-air interface (at z=$L(t)$), which corresponds to the film thickness, the mass balance from diffusion and evaporation yields a moving boundary condition,

$$\boldsymbol{D_{eff}} \frac{\partial \boldsymbol{C}}{\partial \boldsymbol{z}} = \boldsymbol{-C} \frac{\partial \boldsymbol{L}}{\partial \boldsymbol{t}} \boldsymbol{\dot{m}} \quad \text{Equation 12}$$

where $\dot{m}$ [mol·m^{-2}·s^{-1}] is the solvent mass flux at the film-air interface, and it is driven by the concentration difference between the interface and the surrounding air,

$$\boldsymbol{\dot{m}} = \boldsymbol{k_c} \cdot (\boldsymbol{C_s - C_a}) \quad \text{Equation 13}$$

where k_c [m·s^{-1}] is the mass transfer coefficient, C_s [mol·m^{-3}] is the interface molar concentration of the solvent, C_a [mol·m^{-3}] is the concentration of the solvent in the dryer air. The respective molar concentrations were estimated from the ideal gas law as,

$$\boldsymbol{C_s} = \frac{\boldsymbol{P_s(T_f)} \cdot \boldsymbol{a_{FH}}}{\boldsymbol{RT_f}};\ \boldsymbol{C_a} = \frac{\boldsymbol{P_s(T_a)} \cdot \boldsymbol{RH}}{\boldsymbol{RT_a}} \quad \text{Equation 14}$$

where P_s [Pa] is the partial pressure of the pure solvent at the corresponding temperatures. The partial pressure is limited by the Flory-Huggins activity coefficient (a_{FH}) for interface concentrations and by relative humidity (RH) for molar concentrations in air. The Flory-Huggins activity coefficient describes the thermodynamic interaction of the solvent-polymer mixtures that reduces the partial pressure of the solvent, this is estimated as,

$$a_{FH} = exp\left(ln(\Phi_s) + \chi \Phi_p^2 + \left(1 - \frac{1}{DP}\right)\Phi_p\right) \quad \text{Equation 15}$$

where, Φ_s [−] is the solvent volume fraction, χ [−] is the polymer-solvent interaction parameter, and DP [−] is the degree of polymerization.

Finally, the time dependent boundary thickness used in Equation (12) is estimated from the mass balance as,

$$\frac{dL}{dt} = -\frac{\dot{m}\, M_s}{\rho_f} \frac{L}{\rho_f} \frac{d\rho_f}{dt} \quad \text{Equation 16}$$

where, M_s [kg·mol^{-1}] is the solvent molar mass, and ρ_f [kg·m^{-3}] is the film density.

2.2.2. Heat balance

The temperature gradient between the slurry and the dryer air drives a convective heat flux into the slurry, rising the slurry temperature towards its equilibrium wet-bulb temperature and accelerating the solvent

evaporation. The resulting heat transport in the slurry is governed by the one-dimensional energy balance as given in Equation (17), which solves for the 1D spatiotemporal profile of temperature of the slurry,

$$\frac{\partial}{\partial t}\left(\rho_f C_p T L\right) + \lambda_{th} L \nabla^2 T = -\dot{m} h_{fg} + \dot{q_{\text{in}}} \quad \text{Equation 17}$$

where Cp [J·kg^{-1}·K^{-1}] is the specific heat capacity, λ_{th} [W·m^{-1}·K^{-1}] is the effective thermal conductivity of the slurry, T [K] is the slurry temperature, L [m] is the slurry thickness, h_{fg} [J·kg^{-1}] is the solvent latent heat of vaporization, and q_{in} is the convective heat flux from the dryer air.

2.2.3. Binder transport

To address the extent of binder migration in the slurry, the model described by Font et al. [9] is incorporated into the current drying kinetics. The transport of binder in the slurry occurs by both diffusion and advection due to solvent transport and the evolution binder concentration over time is expressed as,

$$\frac{\partial c_b}{\partial t} = v\frac{\partial c_b}{\partial z} + \frac{\partial}{\partial z}\left(D\frac{\partial c_b}{\partial z}\right) \quad \text{Equation 18}$$

where c_b [mol·m^{-3}] is the concentration of the binder, D [m^2·s^{-1}] is the binder diffusion coefficient, v [m·s^{-1}] is the local solvent velocity arising from the evaporation and the shrinkage of the film. The local solvent velocity was estimated from the mass balance between solvent and solid phases assuming homogeneous distribution of the solid phase and is expressed as [9],

$$v = -\frac{(1-\phi_s)z}{\phi_s L}\frac{dL}{dt} \quad \text{Equation 19}$$

where, ϕ_s [−] is the solvent volume fraction.

2.3. 3D particle-resolved model at the mesoscale

At the mesoscale, the 3D motion of particles during drying was simulated using the CGMD approach via the LAMMPS software [36]. In this approach, the displacement of each particle is governed by Newton's equations of motion while the centre of mass of the particles is tracked,

$$m_i\frac{d^2 r_i}{dt^2} = F_i \quad \text{Equation 20}$$

where r_i is the particle position, m_i its mass and F_i is the total force acting on the particle i. This total force ($_{Fi}$) is a sum of all the interaction forces on the particle i and is composed of interparticle forces (F_{ij}), particle-wall interaction forces ($F_{wall,i}$) and the external forces ($F_{ext,i}$),

$$F_i = \sum_{j\neq i} F_{ij} + F_{wall,i} + F_{ext,i} \quad \text{Equation 21}$$

Two force fields (FFs) were used to describe the interparticle interactions within primary AM and CBSA/CBD particles. First, the Lennard Jones potentials were used to account for non-bonded interactions, representing both short-range repulsion and long-range attraction between any pair of particles within a defined cut-off distance. In addition to this, the Hertz Johnson Kendall Roberts (Hertz-JKR) contact model was applied when particles came into contact or slightly overlapped to describe the adhesive and elastic responses. The Hertz-JKR force incorporates both normal and tangential components including contributions from surface adhesion, viscoelastic damping, and tangential friction. Apart from the interparticle interactions, cohesion between the particles and the current collector at the bottom of the microstructure was also represented using Hertz-JKR FFs. In addition to these, the net external force due to evaporation was implemented considering the local velocity field of the solvent, as estimated from Equation (19).

3. Results and discussion

The results section is organised as follows. First, we present the macroscale model results, where the local ambient conditions in the pilot line are assessed (Section 3.1). These ambient conditions are fed to the 1D drying kinetics model to determine the solvent evaporation rates (Section 3.2). Finally, in Section 3.3, these evaporation profiles are applied to the mesoscale CGMD model (starting from the equilibrated slurry microstructure presented in our previous work [27]) to resolve for the resulting CBD migration and the resulting dried electrode microstructures.

3.1. Heterogeneities in drying machine conditions of the pilot lines

The design of the dryer machine has a direct impact on the hot air circulation inside it. For the macroscale model developed here, the global dimensions of a pilot line convective dryer (present at our Laboratoire de Réactivité et de Chimie des Solides in Amiens) were followed, as shown in Fig. 2. The complexities of different components inside the dryer machine are simplified for the purpose of this study. This design consists of two sequential drying chambers, with alternating air inlets, both on the top and bottom surface of the slurry film along with an air outlet at the top of each drying chamber. These air inlets allow to control the velocity and temperature of the air flowing inside the dryer. The fluid region is modelled as a compressible perfect gas, with constant thermophysical properties for the computational efficiency. The thermophysical properties of the fluid and the solid region used for this model are provided in Tables S1 and S2 of the Supporting Information.

In our case, three possible combinations of inlet temperatures were considered. These combinations follow the standard experimental protocols, where the temperatures in the first dryer chamber are maintained lower than in the second one. Based on typical processing windows for NMP-based slurries, the selected temperature combinations were 343-373 K, 343-393 K, and 373-393 K. The inlet velocities were kept the same in both chambers with a constant value of 1 m s^{-1}. The simulation was run until the flow fields were equilibrated and the chamber temperatures reached the respective set values.

Although the velocity and temperature gradients exist throughout the dryer, the analysis focuses on the region immediately adjacent to the electrode coating surface, as this directly influences the drying rates. Fig. 3a and b show the spatial variation of the temperature and the velocity fields along the dryer machine in the region close to the electrode coating. The temperature distribution within the dryer remains largely uniform in each chamber. In contrast, the velocity field exhibits localised fluctuations, particularly when the electrode passes beneath the inlets and between successive drying chambers (see Fig. 3a). These local variations arise from the perpendicular orientation of the inlets relative to the electrode surface. The corresponding flow field vectors, shown in Fig. S1 of the Supporting Information, indicate the presence of two distinct flow regimes: a confined impinging jet region immediately below the inlets that rapidly transitions into a parallel flow over the adjacent regions. In industrial drying systems, inlet nozzles are usually inclined to reduce direct impingement, thereby minimising mechanical stress on the coating that can lead to defects. The perpendicular configuration adopted in this idealised dryer geometry therefore represents a simplified approximation, and the resulting flow non-uniformities should be interpreted accordingly. Optimising inlet orientation to minimise these variations remains an important design consideration and is identified as a direction for future refinement of the macroscale model, though it remains out of the scope of this article.

The spatial variation along the length of the dryer (2.5 m) is converted into a temporal variation using a constant dryer line speed of 5 mm s^{-1} from entry to exit, which takes 500 s. Fig. 3c and d show the flow field variations along the length (x-axis) at three locations across the width (centre Y:0.00 m; intermediate Y:0.05 m; and edge Y:0.10 m) of

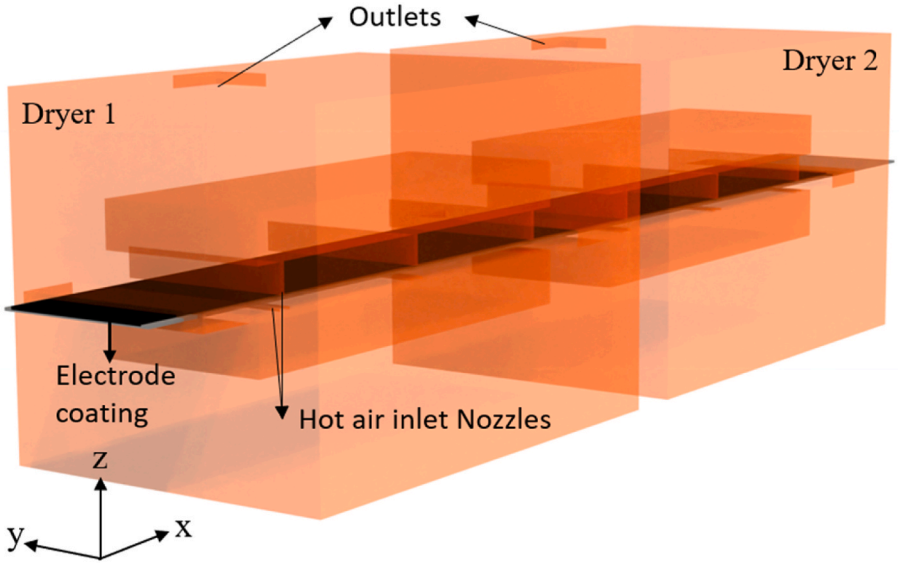

Fig. 2. Design of the chamber pilot scale dryer, composed of two dryers with three alternating air inlets nozzles, both on the top and bottom of the electrode coating, and two outlets at the top.

the film, for the 343-373 K configuration. The magnitudes of velocities along three selected regions vary between 0.1 and 1.4 m s^{-1}. The sharp fluctuation observed near the inlet regions is the stagnation effect of the impinging jet. The temperature and flow field variations at the bottom part of the electrode and the data corresponding to the other configurations of drying temperatures are provided in Figs. S2 and S3 of the Supporting Information. For the heterogeneities observed across the width of the coating, minor variations are presented (within 20 cm of the coating width) in both the temperature and air velocities (Fig. 3a and b).

3.2. Evaluation of drying kinetics

The slurry formulation was composed of solid content (96 % NMC111, 2 % carbon black (C65), 2 % PVdF binder) dispersed in NMP solvent. The initial microstructures for this slurry formulation were derived from equilibrated microstructures previously obtained by us [27], where the 3D slurry microstructure equilibration was conducted using an NPT (isothermal-isobaric) ensemble in CGMD to achieve the experimentally validated (from μ-CT) density of the slurry microstructure. In this section, we investigated five distinct microstructures (referred as St1, St2, St3, St4, and St5), and the solvent content in each case is the effective pore volume obtained after the voxelization of these CGMD structures (with a resolution of 0.2 μm) and these values are presented in Table 1. These microstructures provide the initial solvent fractions and slurry heights required for the 1D drying model. We first establish a baseline using constant drying rates, which is essential for calibrating the mesoscale migration forces in Section 3.3. Later, we integrate the local fluctuations derived from the macroscale CFD model.

3.2.1. Drying kinetics for constant drying rates

The investigation of slurry drying kinetics was primarily conducted by varying the ambient temperature parameter of the 1D model. This is due to its dominant effect on the drying process. While the drying behaviour also depends on the coupled effects of air temperature, velocity, and relative humidity, the scope of this discussion is focused on the thermal influence for clarity, fixing all the other conditions. These assumptions are based on the results we provided in Fig. S4 of the Supporting Information, where we explore the impact of varying air velocities and relative humidity.

Three drying conditions were simulated at different ambient temperatures of 343 K, 373 K, and 393 K under a constant air velocity of 1 m s^{-1} and a relative humidity of 25 %. These conditions were selected to represent low, intermediate, and high temperature conditions, typically encountered in drying of slurries based on NMP solvent [8]. These temperatures resulted in average solvent removal rates of 0.0337, 0.119, and 0.228 g m^{-2} s^{-1}, respectively. Fig. 4a presents the evolution of solvent content in the slurry film under these drying conditions. In all three tested conditions, the curves can be divided into two main stages. Initially, during the constant rate period, the solvent curves show a faster decrease. The mean velocities of the interface for each drying rate in this stage were approximately 8.54×10^{-8}, 3.31×10^{-7}, and 6.67×10^{-7} m s^{-1}, respectively. In the second stage, referred as the falling-rate period, the solvent removal became slower, taking an increasingly longer time to remove the remaining amount of the solvent. During this falling-rate period, the considered 1D model does not explicitly capture the solvent removal through the porous structure. However, the global drying kinetics are captured by considering that the diffusion coefficient and the partial pressure of the solvent (according to Equation (15)) depend on the solvent fraction which results in gradually decaying solvent removal rates. The total drying durations required to reach the final solvent content (of 10 mol m^{-3}) were predicted to be approximately 730 s, 220 s, and 120 s for 343 K, 373 K, and 393 K, respectively. For these drying simulation times, the falling-rate period takes more than three times as long as the constant rate period.

For the slurry formulation considered, the pore volume fraction of the structures formed at the end of the homogeneous drying were considered. The effective solvent filled pore volume for these structures was estimated to be around 27-30 %. Considering the electrode slurry is saturated with the solvent at this point, we can mark the end of film (EOF) shrinkage (shown as the zoom-in section of Fig. 4a) beyond which there is no change in the electrode thickness. The model predictions for normalised binder distribution at the EOF is presented in Fig. 4b. For the higher drying rates with fixed diffusion coefficient of the binder, the rapid removal of the solvent before the EOF resulted in higher migration, resulting in a higher amount of binder located at the top surface of the film. While for the low drying rates, the migration estimated from the 1D model was not significant leading to a more homogeneous distribution.

3.2.2. Impact of macroscale heterogeneities on localised drying rates

The local variations in ambient boundary conditions (in terms of air temperature and velocity), derived from the macroscale dryer model (from Section 3.1), were integrated into the 1D model through time-dependent heat and mass transfer coefficients (for details on their

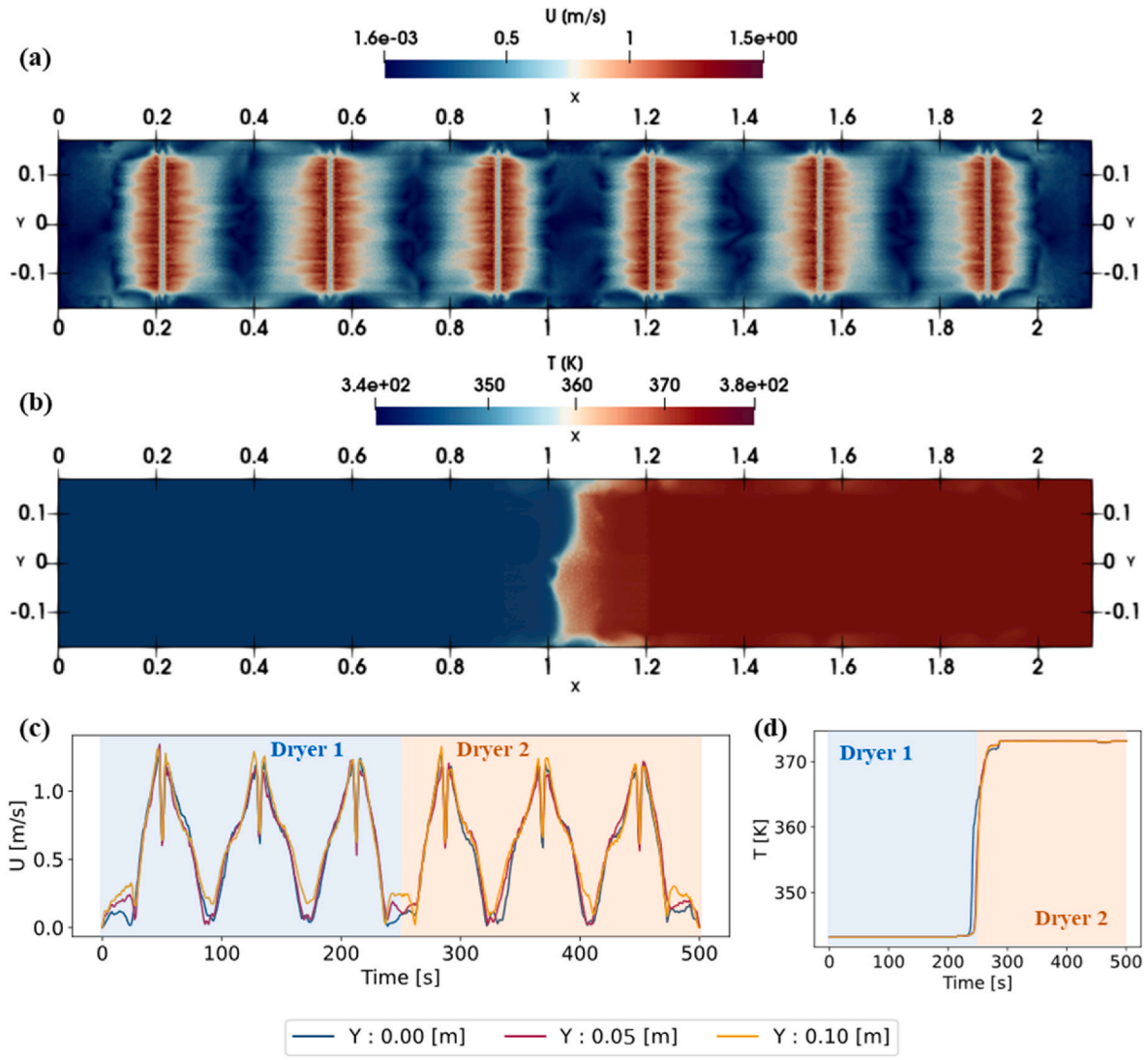

Fig. 3. Computed flow field distributions in the dryer machine obtained by the macroscale model for (a) air velocity and (b) temperature on the top of the slurry film. Local variations at specific regions of the coating surface as it goes through the dryer machine for (c) air velocity, and (d) temperature.

Table 1
Initial properties of the slurry equilibrated microstructures considered as initial microstructures for the drying simulation at the mesoscale in this work (taken from our previous work [27]).

structure	Slurry heights [μm]	Pore volume fraction [−]
St1	77	0.41
St2	76	0.38
St3	76	0.38
St4	81	0.46
St5	76	0.37

evolution, refer to Section S5 of the Supporting Information). Due to the dominant effect of the airflow velocities, the temporal evolution of the transfer coefficients closely resembles the evolution of airflow velocity. The convective heat and mass transfer coefficients are estimated using flat-plate correlations for forced convection (Equation (5) and Equation (7)). While localised impinging flow occurs near the inlets (as presented in Section 3.1), the CFD results (Fig. 3 and Fig. S1) demonstrate that these impingement zones are spatially limited to approximately 8 % of the electrode length. Beyond these zones, the flow transitions rapidly to a parallel regime. Consequently, the impinging jet characteristics apply to less than 2 % of the total drying time. A sensitivity analysis was conducted to address the potential bias introduced by this simplification (refer to Section S7 of the Supporting Information, Figs. S8 and S9). Even assuming that the local transfer coefficients under the jet are two times higher than the flat-plate values, the integrated impact on the total drying time and solvent removal at the end of film shrinkage is estimated to be less than 1 %, which is negligible within the tested range.

The resulting evolution of the solvent fraction in the slurry film, across three locations (corresponding to the centre and longitudinal borders), are presented in Fig. 5a for the whole drying process. Solvent evolution corresponding to the other drying conditions are presented in section S6 of the Supporting Information. The solvent evolution profiles indicate that lateral variations in drying kinetics across the electrode width were negligible, with the exception of the extreme peripheral regions. Evaporation rates at the lateral edges were accelerated compared to the bulk central region. This observation is consistent with minor fluctuations in the transfer coefficients, as the transverse airflow between inlets becomes more pronounced at the coating edges. Across the longitudinal axis (length of the dryer) the air flow velocity varied from approximately 0.1-1.4 m s^{-1} (corresponding to k_c of 1.5×10^{-4} to 2×10^{-3} m s^{-1} and a h_t of 2 to 45 W m^{-1} K^{-1} for the 343-373 K configuration) in all the three cases as presented in Fig. 3c and Figure S5, S6 of Supporting Information. This variation along the length resulted in a cascaded solvent removal with maximum at near to the nozzles and

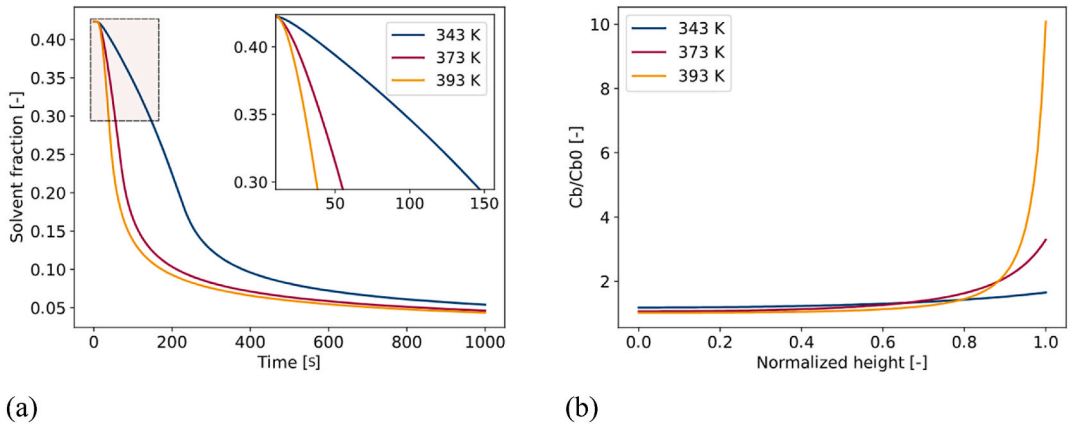

Fig. 4. Drying kinetics model results: (a) Evolution of solvent fraction in the slurry for the different ambient temperature conditions; with zoom-in section presenting the solvent removal before the end of film shrinkage. (b) Vertical binder concentration profiles for different drying rates at the end of film shrinkage.

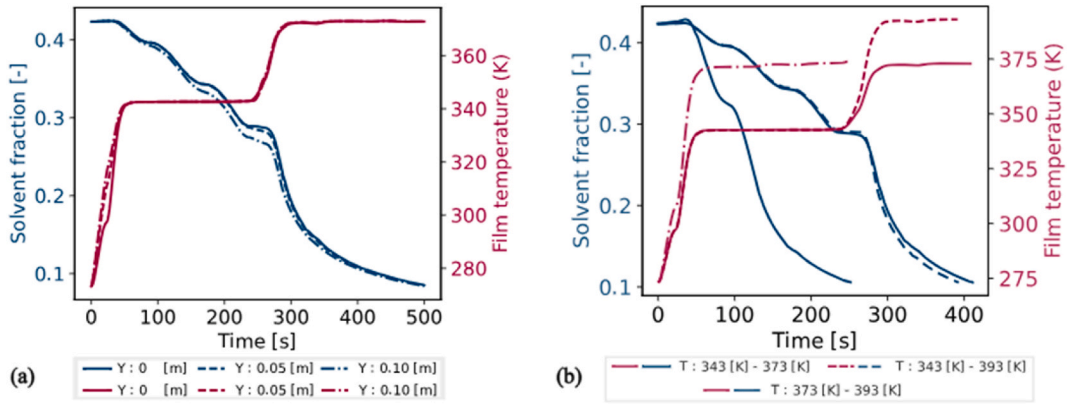

Fig. 5. (a) Evolution of solvent fraction at the three different locations along the width of the electrode (centre, intermediate and edge of the slurry as presented in Fig. 3). (b) Solvent fraction and temperature evolution for the three combinations of temperatures (343-373 K, 343-393 K, and 373-393 K) in the dryer.

almost no evaporation in between two inlet nozzles. This led to an extended drying duration compared to those estimated from constant drying conditions presented earlier. Furthermore, the time required to attain the wet-bulb temperature was delayed in the pilot line. This delay is attributed to also the gradual imposition of initial temperature and velocity in the pilot line model, contrasting with the instantaneous

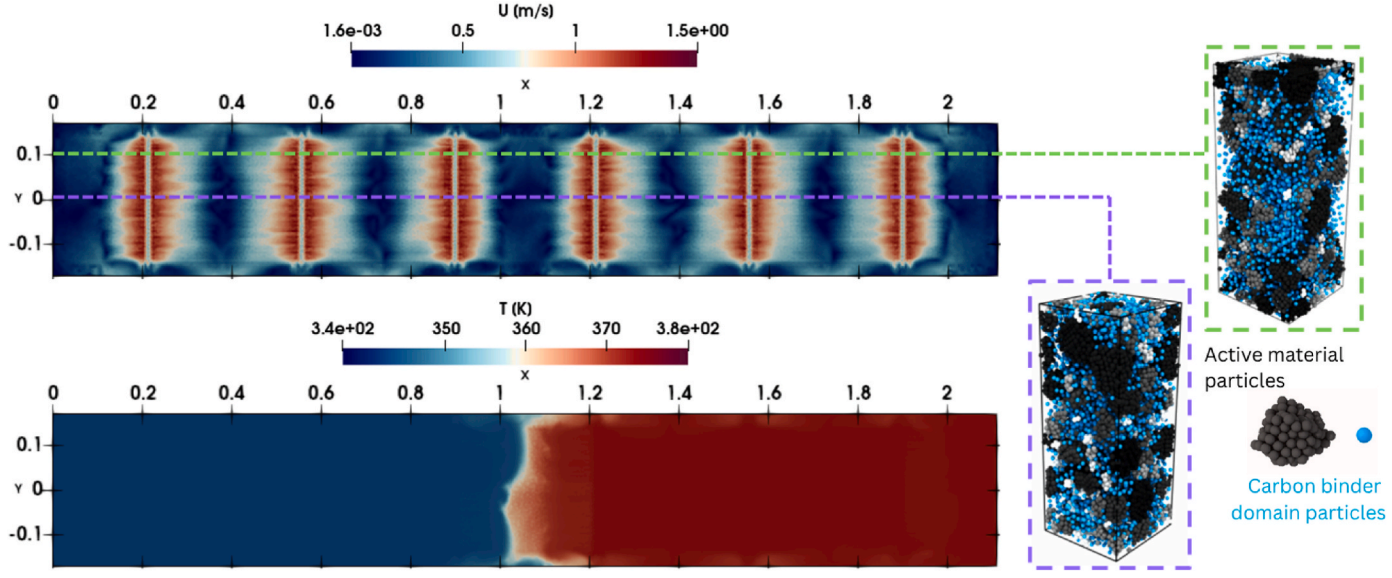

Fig. 6. Macroscale heterogeneities in the slurry films are connected to the 3D mesoscale model, and the predicted dried electrode microstructure are displayed for two different locations.

imposition of fixed temperatures and velocities utilised in the constant drying case in section 3.2.1.

Fig. 5b illustrates the time evolution of the solvent fraction in the slurry coating during the drying process, for selected dryer temperature combinations (343-373 K; 343-393 K; 373-393 K), until achieving a final solvent fraction of 0.1 (beyond which the solvent removal becomes asymptotic and is not of the interest for the migration study later). For the first two temperature profiles, the constant rate period (at the estimated 0.3 solvent fraction) predominantly concluded near the exit of the first dryer stage, transitioning into the falling rate period within the second stage. Insignificant variation in drying time was observed between these two cases in the second stage. The third temperature profile (373-393 K) facilitated reaching the target solvent fraction (of 0.1) upon completion of the first dryer stage.

3.3. Mesoscale model for resolving the binder migration

Fig. 6 shows the connections between the macroscale heterogeneities with the mesoscale model. Two different regions of the slurry film are marked, and the 3D microstructure of the dried electrodes obtained using the mesoscale model is displayed at the end of the line.

We set different temperatures in the macroscale model for the first dryer (343 K, 343 K, 373 K), combined with different ones in the second dryer (373 K, 393 K, 393 K), giving the combinations 343-373 K, 343-393 K, and 373-393 K. For these three air temperature configurations, the solvent concentration profile is obtained at different regions of the slurry film (edge, intermediate and central region) with the 1D model. These heterogeneities are then used as inputs in our mesoscale model to resolve in 3D the arrangement of the particles (AM and CBD), to analyse how these variations affect the binder migration.

For the mesoscale model, the simulated system is composed of NMC AM secondary particles, with realistic shapes (extracted from tomography data) represented by primary spherical particles, and the CBD explicitly modelled as spherical particles. The size and quantity of the CBD particles were determined by accounting for their inherent nanoporosity (estimated at 50 %) and their weight fraction within the formulation. Starting from the equilibrated slurry structures presented in Table 1, solvent removal was modelled by implementing time-dependent solvent evaporation profiles obtained from the 1D model in Section 3.2. The FF parameters governing AM-AM, CBD-CBD, and AM-CBD cohesion interactions were progressively adjusted as a function of the solvent fraction. The evolution is implemented using linear interpolation between the wet (slurry) and dry state, such that each interaction parameter (ψ) follows,

$$\psi(t) = \psi_{wet} + \left(\psi_{dry} - \psi_{wet}\right)\left(1 - \left(\phi_s(t) / \phi_{s0}\right)\right) \quad \text{Equation 22}$$

where $\psi(t)$ is the instantaneous interaction parameter, ψ_{wet} is the value corresponding to the slurry, ψ_{dry} is the value corresponding to the dry state, and $\phi_s(t)$ and ϕ_{s0} are the instantaneous and initial solvent fractions from the 1D model, respectively. As the solvent fraction decreases, the effective interparticle interactions evolve dynamically, capturing the transition from slurry to a dried state. The slurry and dry interaction parameters were adopted from our previous work, where these interactions were calibrated with the experimental data on slurry density and electrode porosity [27]. The corresponding FF interaction values are presented in Table S4 of the Supporting Information. The evolution of the cohesive interaction parameters is phenomenological, assuming that the increase in cohesion strength is directly correlated with solvent depletion in the slurry, consistent with the progressive formation of solid-to-solid contacts as the liquid phase diminishes. Other modelling details, such as particle size distribution and number of AM and CBD particles, are already available in our previous work [27].

To model the migration of CBD within the slurry microstructure, an evaporation induced advection force was applied to the CBD particles, in addition to the previously mentioned interparticle interaction forces. Given the high viscosity of the polymer-solvent system and the relatively small particle sizes, the characteristic timescales of other body forces, such as the gravitational and buoyancy effects, were estimated to be negligible compared to that of the evaporation induced advection force. During the constant-rate drying regime, the velocity of the evaporation front is estimated from a solvent mass balance using the instantaneous solvent fraction in the slurry. This global front velocity is imposed as a boundary condition to displace the slurry-air interface. Subsequently, to drive particle displacement, the front velocity is distributed along the microstructure as the local fluid velocity according to Equation (19) presented in Section 2. The local Stokes drag force experienced by particles can be expressed as,

$$F_{\mathrm{drag}} = 6\pi\eta r\, V_{\mathrm{rel}} \quad \text{Equation 23}$$

where η is the solvent viscosity, r is the particle radius, and V_{rel} is the relative velocity between the particle and the surrounding solvent. Since evaporation is primarily a surface phenomenon, the solvent velocity is assumed to vary linearly across the electrode thickness. Due to the intrinsic consideration of viscosity because of the interparticle FFs, the drag force coefficient was validated using the solvent removal profiles from the constant drying rate kinetics. The applied local velocity field represents a spatially averaged approximation rather than a fully resolved 3D local flow field. Consequently, local hydrodynamic effects, such as lateral flow redistribution, pore-scale acceleration, and recirculation within tortuous pathways, are not explicitly captured with this model which is beyond the scope of the current work. Fig. 7a-c illustrate the evolution of the CGMD microstructure as the solvent is removed. The migration of the CBD particles with respect to this solvent removal is presented in the Supporting Videos S1-S5.

Fig. 7 d and e show the spatial redistribution of the CBD particles in the dried electrode microstructure under selected constant drying rate conditions, specifically for low drying rate (LDR) case (drying kinetics corresponding to 343 K case) (Fig. 7d) and the high drying rate (HDR) case (drying kinetics of 393K) (Fig. 7e). This analysis was performed for each drying scenario on five different initial slurry microstructures. For the LDR condition, the rate of solvent removal was slow, which facilitated a consistently homogeneous dried electrode microstructure characterised by minimal vertical segregation of the CBD particles throughout the electrode thickness. Conversely, the HDR condition resulted in a pronounced heterogeneity in the dried electrode microstructure. Specifically, a significant depletion of CBD was observed in the bottom region of the electrode, corresponding to a higher accumulation near the electrode's surface.

The estimated overall migration of CBD particles derived from the 3D microstructures was lower than the 1D estimates presented in Fig. 4b in Section 3.2.1. This is due to the limited transport of CBD particles within the tortuous pore network, while 1D models, on the other hand, assume a free path to the surface. To quantify this point, the pore throat size distribution of the evolving 3D microstructures was quantified using the bubble point method of GeoDict. The most constrictive pore throat diameters decreased from 12 μm, in the wet slurry state, to 1.3 μm, in the dried microstructure. Therefore, before the AM skeleton is formed, the individual diameter of the CBD particles is sufficiently small to escape any artificial entrapment effect. Nevertheless, CBD clusters (forming due to the increasing cohesion from the wet to dry states) can be trapped near the pore throats when solvent removal is faster, and the CBD clusters attach to the AM surface.

Table 2 shows the porosity, the tortuosity factor and the relative conductivity fraction (relative to a fully CBD conductive microstructure) for the different drying temperatures. These properties were calculated with the dried electrode microstructure obtained at the end of the mesoscale CGMD simulation by using GeoDict (Math2Market) [37]. To be able to use this software, we performed an intermediate step that involved the voxelization of the microstructure with an in-house Python code. The size of each voxel was set to 0.2 μm. To calculate the electrode porosity (ε) the number of pores' voxels are added to a fraction of the

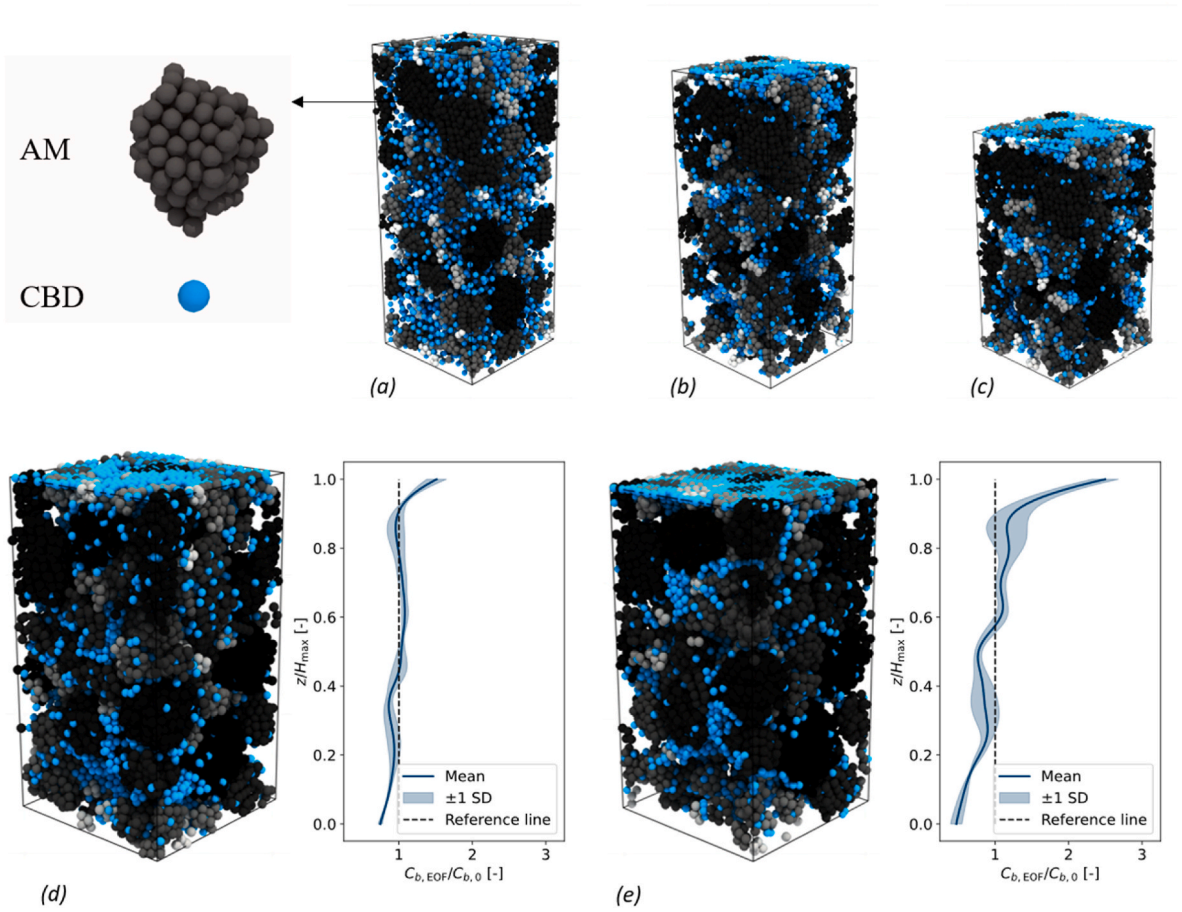

Fig. 7. Snapshots of the time evolution of electrode microstructure during the slurry drying process showing the realistic AM shapes and CBD at: (a) initial slurry structure (b) partially removed solvent (c) end of drying. Microstructures of the dried electrode aligned with the binder profiles relative to the initial distribution, for the drying temperature conditions of: (d) low drying rate (LDR): 343 K, and (e) high drying (HDR): 393 K (the respective uncertainty zone (one standard deviation (±1 SD)) are computed over simulations with five different initial slurry microstructures).

Table 2
Computation of porosity, tortuosity factor, and relative conductivity fraction for the predicted electrode microstructure obtained with the different conditions in terms of temperature.

Drying temperature	Porosity	Tortuosity factor	Relative conductivity fraction
343 K	0.26 ± 0.03	2.93 ± 0.22	0.0014 ± 0.0002
373 K	0.26 ± 0.03	4.37 ± 0.23	0.0010 ± 0.0002
393 K	0.27 ± 0.03	4.75 ± 0.47	0.0009 ± 0.0002

number of CBDs' voxels (accounting for its nanoporosity) and divided by the total number of voxels. The tortuosity factor (τ) is estimated as the ratio of porosity to effective diffusivity ($\tau = \varepsilon/D_{eff}$), based on the Mac-Mullin number equation [38]. Here, the diffusion coefficient within the pores is assumed to be 1, while the effective electrode diffusivity (D_{eff}) is obtained by solving Fick's laws for the pore network. Then, the conductivity is obtained through solving the Poisson equation in the conductive domain and then applying the Ohm's law. We have already provided more details about the assumptions, parameters, and boundary conditions in our previous works [28,34,39]. As presented in Table 2, the mean porosity of the dried electrode microstructure does not present changes when the drying temperature is increased. Then, for the lowest drying temperature (343 K), the mean tortuosity factor is the lowest and the relative conductivity fraction the highest. Lastly, for both 373 K and 393 K the values of tortuosity factor and relative conductivity fraction do not present appreciable changes.

To bridge the macroscale drying heterogeneities with mesoscale structural evolution, the solvent evaporation profiles derived from the dryer simulations (Section 3.2.2) were implemented as boundary conditions for the mesoscale model. Fig. 8a–c shows the spatial variability in the migration of the CBD phase from the centre of the dried electrode film (Y:0 [m]) to its lateral edge (Y: 0.1 [m]). The extent of migration in each of these cases follows the general trends described for the constant drying rates. In case of the 343–373 K, the spatial variations in temperature and airflow velocity were more pronounced than in the higher temperature cases (343–393 K and 373–393 K, respectively), resulting in increased lateral heterogeneity in binder distribution. This sensitivity at lower dryer temperatures can be attributed to a reduced advection force on the CBD phase. Under these conditions, the particles remain mobile for an extended duration, rendering their final distribution highly susceptible to localised drying fluctuations. In contrast, high evaporation rates generate strong advective force that rapidly locks the CBD particles within the pores and onto the AM surfaces, thereby suppressing migration variability across the lateral direction. Furthermore, Fig. 8d–f shows the influence of variations in the initial microstructure on migration under different drying conditions. For the low temperature cases in the first dryer (both 343-373 K and 343-393 K) the migration terminates in the first dryer which leads to no significant differences in the binder distribution along the thickness. The high temperature (373-393 K) case exhibited greater sensitivity to initial structural variations by showing greater variations in its error curve. As established previously in section 3.3, the rapid entrapment at elevated temperatures can amplify the microstructural differences that are coming from the initial distribution,

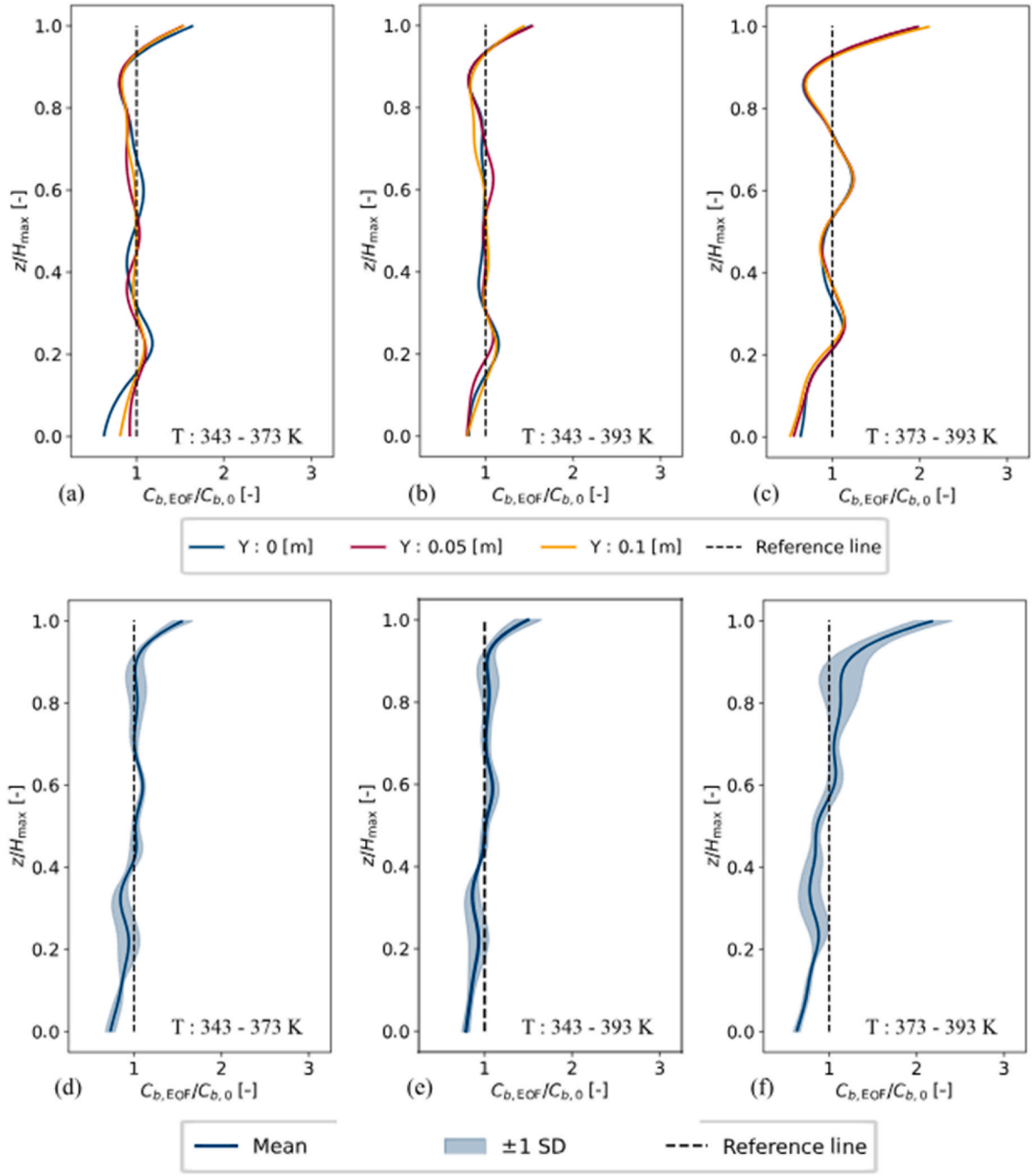

Fig. 8. Binder migration behaviour on the 3D electrode microstructures for the various drying temperature configurations. Variability in binder migration along the lateral direction on the electrode (centre, intermediate and edge), with a width 20 cm, for the temperature configurations of: (a) 343-373 K, (b) 343-393 K, and (c) 373-393 K (the reference line indicates the binder location in the slurry microstructure). Variability in binder migration due to the change in the initial slurry microstructure for the temperature configurations of: (d) 343-373 K, (e) 343-393 K, and (f) 373-393 K (±1 SD refers to the standard deviation that determines the uncertainty zone).

leading to a more heterogeneous binder network compared to the low temperature case. Such spatial differences ultimately demonstrate a non-uniform mechanical strength that can lead to localised delamination.

Finally, the porosity, tortuosity factor, and relative conductivity fraction of the obtained dried electrode microstructures were computed using the details given in the previous Section 3.3, based on the conditions set by the macroscale model (representing the drying machine). These values are presented in Table 3 to determine how the dryer temperature configuration affects the average dried electrode properties. The average and standard deviation for porosities are the same for

Table 3
Average and standard deviation of porosity, tortuosity factor, and relative conductivity fraction for the dried electrode microstructures obtained from the simulations with the different temperature configurations in the dryer machine.

Drying temperature	Porosity	Tortuosity factor	Relative conductivity fraction
343-373 K	0.26 ± 0.03	2.90 ± 0.22	0.0013 ± 0.0001
343-393 K	0.26 ± 0.03	2.87 ± 0.20	0.0015 ± 0.0003
373-393 K	0.26 ± 0.03	3.73 ± 0.25	0.0012 ± 0.0003

the three different configurations. This implies that this property is unaffected by the drying machine conditions and is instead defined by the parameters from the previous manufacturing step, such as the AM-CBD formulation ratio. Then, we found complementary behaviours for the tortuosity factors and the fraction of relative conductivities. For the former, there is a minimum for the 343-393 K condition, whereas for the latter, there is a maximum. As explained earlier in this section, the film shrinks before exiting the first dryer chamber at a temperature setting of 343 K. Consequently, migration is limited, and when these conditions encounter the higher temperatures of the second dryer at 373 K, the FF strengthens more slowly than in the case where the second dryer temperature is 393 K. This sets the optimal drying temperature condition at 343-393 K, offering the best compromise between minimum tortuosity factor and maximum relative conductivity fraction.

To the best of our knowledge, the modelling framework that we present in this work, which combines different simulation scales, is the first of its kind. It can predict the effect of the conditions set on the machinery at the slurry drying step on the mesoscopic properties of the electrodes. Furthermore, it enables the simultaneous analysis of macroscopic heterogeneities and the microstructural configurations.

4. Conclusions and perspectives

In this article, we presented a modelling approach that couples different scales and can predict the effects of macroscale slurry drying heterogeneities on the properties of the final electrode microstructures. To the best of our knowledge, this is the first reported instance of a framework that links macroscale slurry dryer dynamics and 3D-resolved slurry/electrode microstructural evolution. Our macroscale CFD simulations revealed that the complex interplay of temperature and airflow fluctuations between dryer inlets results in a cascaded removal of solvent. This led to longer drying times than anticipated under idealised, constant drying conditions. Furthermore, the model captures the edge effects of the electrode coating, where circulation led to more gradual airflow variations and accelerated solvent removal in specific areas.

By integrating the solvent evaporation profiles from the macroscale into our 3D-resolved CGMD model, we have demonstrated the predictive capability regarding the extent of CBD migration under varying drying conditions. By comparing extreme drying regimes, we observed that high drying rates drive the migration of the CBD phase toward the evaporation surface, leading to its depletion at the current collector interface. For the tested conditions we also observed that the predictions of migration in the 3D resolved model were much lower compared to the ones from 1D model. This is hypothesised to be due to the free flow assumptions inherent in the 1D model, which fails to account for the complex tortuous skeleton defined by the realistic-shape AM particles. In the actual 3D microstructure, the transport of CBD particles is hindered by the physical arrangement of AM particles, leading to local entrapment of CBD clusters formed during solvent removal. This can create localised heterogeneities in the distribution of the binder that can result in a lower performance of the electrodes. The model framework also predicts the variability expected in the electrode properties across the width of the coating thanks to the integration of multiple scales with the local flow fields in the dryer. We showed that, in the case of a high drying rate, the initial configuration of AM and CBD particles results in higher variability in the binder migration. For the similar initial microstructures, we found that the low drying rates can become more sensitive to the local flow variations in the dryer.

As a future perspective of our work, the proposed modelling approach could be used to optimise the design of the dryer machine to minimise the heterogeneities along the electrode film. For example, we could find the optimal inclination of the inlet nozzles to minimise the local variability of the flow non-uniformities. In the current 3D-resolved mesoscale model, the advective transport of the CBD phase is governed by a thickness-averaged evaporation front velocity that is applied throughout the film shrinkage stage. While this approximation captures the dominant drying behaviour, it neglects local hydrodynamic phenomena, such as flow redistribution and pore-scale acceleration, during the initial stages of drying. A fully coupled CFD-DEM approach at the mesoscale could be adopted to address these limitations, enabling explicit resolution of local velocity fields. However, this approach would result in a significantly higher computational cost. In addition to this, the model assumes negligible CBD migration during the second drying stage, when two-phase transport effects are minimal. While this assumption is valid for thin coatings, it becomes less accurate for thicker slurry films, where continued transport within the porous network may be significant and would similarly require a CFD-DEM coupled approach at the mesoscale. Furthermore, the computational cost of the mesoscale model could be decreased, by maintaining a high accuracy, by using our previous physics-assisted ML surrogate model for the slurry drying step [28]. Similar approaches could be implemented for the models at the other scales to derive physics- and chemistry-informed AI models, providing an optimal balance between accuracy and computational cost. This would allow to perform inverse design considering many of the parameters addressed in this work (such as air temperature and velocity). Finally, this framework paves the way to a digital twin of the drying stage by providing a digital model that could be used in its core to interact in a real-time, automated, and bidirectional way with the drying machinery for its parameter optimisation.

CRediT authorship contribution statement

Abhilash Valisammagari: Conceptualization, Data curation, Formal analysis, Investigation, Methodology, Software, Validation, Visualization, Writing – original draft. **Francisco Fernandez:** Conceptualization, Formal analysis, Investigation, Methodology, Validation, Writing – original draft. **Mohammed Alabdali:** Conceptualization, Formal analysis, Investigation, Methodology, Writing – original draft. **Alejandro A. Franco:** Conceptualization, Funding acquisition, Methodology, Project administration, Resources, Supervision, Writing – review & editing.

Declaration of competing interest

The authors declare that they have no known competing financial interests or personal relationships that could have appeared to influence the work reported in this paper.

Acknowledgements

A.A.F., F.F., and A.V. acknowledge financial support from the EU Horizon Europe project DigiCell (Grant Agreement no. 101135486). A. A.F. and M.A. acknowledge the European Union's Horizon Europe research and innovation program under grant agreement no. 101069686 (PULSELiON). A.A.F. acknowledges the funding support of the French National Research Agency under the France 2030 program (Grant ANR-22-PEBA-0002, PEPR project “BATMAN”). The authors also acknowledge the MatriCS HPC platform from Université de Picardie Jules Verne on which the simulations were performed. A.A.F. acknowledges Institut Universitaire de France for the support.

Appendix A. Supplementary data

Supplementary data to this article can be found online at https://doi.org/10.1016/j.jpowsour.2026.240481.

Data availability

Data will be made available upon reasonable request.

References

[1] G.E. Blomgren, The development and future of lithium ion batteries, J. Electrochem. Soc. 164 (1) (2017) A5019–A5025, https://doi.org/10.1149/2.0251701jes.

[2] Y. Liu, R. Zhang, J. Wang, Y. Wang, Current and future lithium-ion battery manufacturing, iScience 24 (4) (2021) 102332, https://doi.org/10.1016/j.isci.2021.102332.

[3] J.-H. Schünemann, H. Dreger, H. Bockholt, A. Kwade, Smart electrode processing for battery cost reduction, ECS Trans. 73 (1) (2016) 153–159, https://doi.org/10.1149/07301.0153ecst.

[4] S.N. Bryntesen, A.H. Strømman, I. Tolstorebrov, P.R. Shearing, J.J. Lamb, O. Stokke Burheim, Opportunities for the state-of-the-art production of LIB electrodes—A review, Energies 14 (5) (2021) 1406, https://doi.org/10.3390/en14051406.

[5] A. Nekahi, E. Feyzi, M. Srivastava, F. Yeganehdoust, A.K. Madikere Raghunagtha Reddy, K. Zaghib, Advanced lithium-ion battery process manufacturing equipment for gigafactories: past, present, and future perspectives, iScience 28 (7) (2025) 112691, https://doi.org/10.1016/j.isci.2025.112691.

[6] Y.S. Zhang, N.E. Courtier, Z. Zhang, K. Liu, J.J. Bailey, A.M. Boyce, G. Richardson, P.R. Shearing, E. Kendrick, D.J.L. Brett, A review of lithium-ion battery electrode drying: mechanisms and metrology, Adv. Energy Mater. 12 (2) (2022) 2102233, https://doi.org/10.1002/aenm.202102233.

[7] M. Lippke, T. Ohnimus, F. Frankenberg, C. Schilde, A. Kwade, Drying and calendering of lithium ion battery electrodes: a combined simulation approach, Powder Technol. 444 (2024) 119984, https://doi.org/10.1016/j.powtec.2024.119984.

[8] N. Susarla, S. Ahmed, D.W. Dees, Modeling and analysis of solvent removal during Li-Ion battery electrode drying, J. Power Sources 378 (2018) 660–670, https://doi.org/10.1016/j.jpowsour.2018.01.007.

[9] F. Font, B. Protas, G. Richardson, J.M. Foster, Binder migration during drying of lithium-ion battery electrodes: modelling and comparison to experiment, J. Power Sources 393 (2018) 177–185, https://doi.org/10.1016/j.jpowsour.2018.04.097.

[10] T. Lombardo, A.C. Ngandjong, A. Belhcen, A.A. Franco, Carbon-binder migration: a three-dimensional drying model for lithium-ion battery electrodes, Energy Storage Mater. 43 (2021) 337–347, https://doi.org/10.1016/j.ensm.2021.09.015.

[11] C. Zihrul, M. Lippke, A. Kwade, Model development for binder migration within lithium-ion battery electrodes during the drying process, Batteries 9 (9) (2023) 455, https://doi.org/10.3390/batteries9090455.

[12] N. Kumano, Y. Yamaguchi, Y. Akimoto, A. Ohshima, H. Nakamura, M. Yamamura, Migration of binder and conductive agent during drying process of Li-Ion battery cathodes, J. Power Sources 591 (2024) 233883, https://doi.org/10.1016/j.jpowsour.2023.233883.

[13] B. Westphal, H. Bockholt, T. Günther, W. Haselrieder, A. Kwade, Influence of convective drying parameters on electrode performance and physical electrode properties, ECS Trans. 64 (22) (2015) 57–68, https://doi.org/10.1149/06422.0057ecst.

[14] M. Baunach, S. Jaiser, S. Schmelzle, H. Nirschl, P. Scharfer, W. Schabel, Delamination behavior of lithium-ion battery anodes: influence of drying temperature during electrode processing, Dry. Technol. 34 (4) (2016) 462–473, https://doi.org/10.1080/07373937.2015.1060497.

[15] M. Müller, L. Pfaffmann, S. Jaiser, M. Baunach, V. Trouillet, F. Scheiba, P. Scharfer, W. Schabel, W. Bauer, Investigation of binder distribution in graphite anodes for lithium-ion batteries, J. Power Sources 340 (2017) 1–5, https://doi.org/10.1016/j.jpowsour.2016.11.051.

[16] L.A. Román-Ramírez, G. Apachitei, M. Faraji-Niri, M. Lain, W.D. Widanage, J. Marco, Understanding the effect of coating-drying operating variables on electrode physical and electrochemical properties of lithium-ion batteries, J. Power Sources 516 (2021) 230689, https://doi.org/10.1016/j.jpowsour.2021.230689.

[17] J. Parker, R. Smith, D. Cumming, High-resolution X-Ray mapping of fluorinated binders in lithium-ion battery electrodes, J. Phys. Chem. C 128 (49) (2024) 20957–20966, https://doi.org/10.1021/acs.jpcc.4c05678.

[18] K. Rollag, D. Juarez-Robles, Z. Du, D.L. Wood, P.P. Mukherjee, Drying temperature and capillarity-driven crack formation in aqueous processing of Li-Ion battery electrodes, ACS Appl. Energy Mater. 2 (6) (2019) 4464–4476, https://doi.org/10.1021/acsaem.9b00704.

[19] S. Jaiser, M. Müller, M. Baunach, W. Bauer, P. Scharfer, W. Schabel, Investigation of film solidification and binder migration during drying of Li-Ion battery anodes, J. Power Sources 318 (2016) 210–219, https://doi.org/10.1016/j.jpowsour.2016.04.018.

[20] S. Jaiser, J. Kumberg, J. Klaver, J.L. Urai, W. Schabel, J. Schmatz, P. Scharfer, Microstructure formation of lithium-ion battery electrodes during drying – an Ex-Situ study using cryogenic broad ion beam slope-cutting and scanning electron microscopy (Cryo-BIB-SEM), J. Power Sources 345 (2017) 97–107, https://doi.org/10.1016/j.jpowsour.2017.01.117.

[21] E. Oppegård, A. Jinasena, A. Hammer Strømman, J. Are Suul, O. Stokke Burheim, Study of an Industrial Electrode Dryer of a Lithium-Ion Battery Manufacturing Plant: Dynamic Modeling, 2021, pp. 77–84, https://doi.org/10.3384/ecp2017677.

[22] J. Kumberg, M. Müller, R. Diehm, S. Spiegel, C. Wachsmann, W. Bauer, P. Scharfer, W. Schabel, Drying of lithium-ion battery anodes for use in high-energy cells: influence of electrode thickness on drying time, adhesion, and crack formation, Energy Tech 7 (11) (2019) 1900722, https://doi.org/10.1002/ente.201900722.

[23] J. Kumberg, M. Baunach, J.C. Eser, A. Altvater, P. Scharfer, W. Schabel, Investigation of drying curves of lithium-ion battery electrodes with a new gravimetrical double-side batch dryer concept including setup characterization and model simulations, Energy Tech 9 (2) (2021) 2000889, https://doi.org/10.1002/ente.202000889.

[24] A. Mesbah, A.N. Ford Versypt, X. Zhu, R.D. Braatz, Nonlinear model-based control of thin-film drying for continuous pharmaceutical manufacturing, Ind. Eng. Chem. Res. 53 (18) (2014) 7447–7460, https://doi.org/10.1021/ie402837c.

[25] M. Stein, A. Mistry, P.P. Mukherjee, Mechanistic understanding of the role of evaporation in electrode processing, J. Electrochem. Soc. 164 (7) (2017) A1616–A1627, https://doi.org/10.1149/2.1271707jes.

[26] D.L. Wood, J.D. Quass, J. Li, S. Ahmed, D. Ventola, C. Daniel, Technical and economic analysis of solvent-based lithium-ion electrode drying with water and NMP, Dry. Technol. 36 (2) (2018) 234–244, https://doi.org/10.1080/07373937.2017.1319855.

[27] J. Xu, A.C. Ngandjong, C. Liu, F.M. Zanotto, O. Arcelus, A. Demortière, A. A. Franco, Lithium ion battery electrode manufacturing model accounting for 3D realistic shapes of active material particles, J. Power Sources 554 (2023) 232294, https://doi.org/10.1016/j.jpowsour.2022.232294.

[28] D.E. Galvez-Aranda, F. Fernandez, A.A. Franco, Physics-assisted machine learning for the simulation of the slurry drying in the manufacturing process of battery electrodes: a hybrid time-dependent VGG16-DEM model, ACS Appl. Mater. Interfaces 17 (22) (2025) 32150–32162, https://doi.org/10.1021/acsami.4c23103.

[29] M. Alabdali, F.M. Zanotto, B. Notredame, V. Viallet, V. Seznec, A.A. Franco, Experimental and computational analysis of slurry-based manufacturing of solid-state battery composite cathode, Batter. Supercaps 8 (2) (2025) e202400709, https://doi.org/10.1002/batt.202400709.

[30] J.F. Troncoso, F.M. Zanotto, D.E. Galvez-Aranda, D. Zapata Dominguez, L. Denisart, A.A. Franco, The ARTISTIC battery manufacturing digitalization initiative: from fundamental research to industrialization, Batter. Supercaps 8 (1) (2025) e202400385, https://doi.org/10.1002/batt.202400385.

[31] D. Zapata Dominguez, J. Xu, Y. Boudjema, S. Ben Hadj Ali, F.M. Zanotto, A. A. Franco, Influence of the mixing speed in the rheology of NMC622-Based Li-Ion battery electrode slurries, Journal of Power Sources Advances 26 (2024) 100141, https://doi.org/10.1016/j.powera.2024.100141.

[32] D.E. Galvez-Aranda, T.L. Dinh, U. Vijay, F.M. Zanotto, A.A. Franco, Time-dependent deep learning manufacturing process model for battery electrode microstructure prediction, Adv. Energy Mater. 14 (15) (2024) 2400376, https://doi.org/10.1002/aenm.202400376.

[33] U. Vijay, D.E. Galvez-Aranda, F.M. Zanotto, T. Le-Dinh, M. Alabdali, M. Asch, A. A. Franco, A hybrid modelling approach coupling physics-based simulation and deep learning for battery electrode manufacturing simulations, Energy Storage Mater. 75 (2025) 103883, https://doi.org/10.1016/j.ensm.2024.103883.

[34] U. Vijay, F. Fernandez, S. Ben Hadj Ali, M. Asch, A.A. Franco, Surrogate modeling of lithium-ion battery electrode manufacturing by combining physics-based simulation and deep learning, Batter. Supercaps (2025) e202500433, https://doi.org/10.1002/batt.202500433.

[35] H.G. Weller, G. Tabor, H. Jasak, C. Fureby, A tensorial approach to computational continuum mechanics using object-oriented techniques, Comput. Phys. 12 (6) (1998) 620–631, https://doi.org/10.1063/1.168744.

[36] S.J. Plimpton, A. Kohlmeyer, A.P. Thompson, S.G. Moore, R. Berger, LAMMPS: Large-scale atomic/molecular massively parallel simulator. https://doi.org/10.5281/ZENODO.3726416, 2023.

[37] Math2Market GmbH, GeoDict Simulation Software Release 2024, Math2Market GmbH, DE, 2024, https://doi.org/10.30423/release.geodict2024.

[38] R.B. MacMullin, G.A. Muccini, Characteristics of porous beds and structures, AIChE J. 2 (3) (1956) 393–403, https://doi.org/10.1002/aic.690020320.

[39] T. Lombardo, F. Lambert, R. Russo, F.M. Zanotto, C. Frayret, G. Toussaint, P. Stevens, M. Becuwe, A.A. Franco, Experimentally validated three-dimensional modeling of organic-based sodium-ion battery electrode manufacturing, Batter. Supercaps 5 (8) (2022) e202200116, https://doi.org/10.1002/batt.202200116.